Demonstration and imaging of cryogenic magneto-thermoelectric cooling in a van der Waals semimetal

T. Völkl[1,4], A. Aharon-Steinberg [1,4], T. Holder [1,2], E. Alpern[1], N. Banu[1], A. K. Pariari[1], Y. Myasoedov[1], M. E. Huber [3], M. Hücker[1] & E. Zeldov [1] ✉

Attaining viable thermoelectric cooling at cryogenic temperatures is of considerable fundamental and technological interest for electronics and quantum materials applications. In-device temperature control can provide more efficient and precise thermal environment management compared with conventional global cooling. The application of a current and perpendicular magnetic field gives rise to cooling by generating electron–hole pairs on one side of the sample and to heating due to their recombination on the opposite side, which is known as the Ettingshausen effect. Here we develop nanoscale cryogenic imaging of the magneto-thermoelectric effect and demonstrate absolute cooling and an Ettingshausen effect in exfoliated WTe_2 Weyl semimetal flakes at liquid He temperatures. In contrast to bulk materials, the cooling is non-monotonic with respect to the magnetic field and device size. Our model of magneto-thermoelectricity in mesoscopic semimetal devices shows that the cooling efficiency and the induced temperature profiles are governed by the interplay between sample geometry, electron–hole recombination length, magnetic field, and flake and substrate heat conductivities. The observations open the way for the direct integration of microscopic thermoelectric cooling and for temperature landscape engineering in van der Waals devices.

Thermoelectric effects have long been used for generating power, cooling electronic devices and measuring temperature where compact size, high stability, vibrationless operation without moving parts and high tunability are required[1,2]. Historically, research efforts have focused on elevated temperatures as the cooling efficiency decreases substantially at lower temperatures, such that it is eventually overshadowed by Joule heating for realistic current strengths. In recent years, the advent of high-purity single-crystal semimetals has led to increased interest in thermoelectric effects at cryogenic temperatures[3–12].

The common approach to thermoelectric cooling is based on the Peltier effect[13], in which a temperature gradient is attained along the current flow direction in structures composed of regions or materials with different Peltier coefficients, which, thus, carry different average amounts of heat per transferred unit charge. Peltier cooling of bulk materials down to liquid nitrogen temperatures has been realized in a number of studies[2,14], with only one report of bulk cooling at liquid He temperatures[15]. By engineering microscopic devices that form energy gaps in the electron density of states, like superconducting junctions or quantum dots, the efficiency of Peltier cooling at very low temperatures

[1]Department of Condensed Matter Physics, Weizmann Institute of Science, Rehovot, Israel. [2]School of Physics and Astronomy, Tel Aviv University, Tel Aviv, Israel. [3]Departments of Physics and Electrical Engineering, University of Colorado Denver, Denver, CO, USA. [4]These authors contributed equally: T. Völkl, A. Aharon-Steinberg. ✉e-mail: eli.zeldov@weizmann.ac.il

can be enhanced substantially due to the preferential transmission of electrons at specific energies[16–18].

Here we address a very different and interesting magneto-electro-thermal mechanism, the Ettingshausen effect[19], which has not been studied in microscopic devices previously[18], and we present the observation of the Ettingshausen effect and Ettingshausen cooling at 4 K. The application of a charge current in the presence of a perpendicular magnetic field leads to a temperature gradient that is transverse to the current flow direction, rather than along it. In a metal, this effect is due to the energy dependence of the drift velocity of the charge carriers, which in the presence of magnetic field, deflects the high- and low-energy carriers to opposite sides of the sample, thus providing heating and cooling upon equilibration of the carriers with the lattice (Fig. 1a). The resulting current to temperature gradient conversion in this case is rather weak.

A much stronger effect can be attained in semiconductors and semimetals hosting both electrons and holes with approximately equal densities and mobilities[18,20]. Under such circumstances, the Hall voltage that usually develops across a device is diminished and the unbalanced Lorentz force drives both the electrons and holes in the same transverse direction (Fig. 1b). This leads to a non-equilibrium electron–hole pair accumulation on one side and depletion on the opposite side. As a result, recombination and generation of electron–hole pairs is increased, thus providing heating and cooling at opposing sides through equilibration with the lattice[19]. As such, heating and cooling are expected to be constrained to a small area within the recombination length l_R from the boundaries. Hence, a thermal measurement technique with spatial resolution on that length scale is required to fully elucidate the effect.

The search for suitable materials for thermoelectric cooling has focused predominantly on bulk systems, leaving the unrecognized potential of mesoscopic devices for integrated cooling largely unexplored[18]. Employing van der Waals (vdW) semimetals as thermoelectric elements[21–26] is especially promising since they can be readily integrated into stacks of atomic layers and moiré heterostructures[27,28]. Herein, different materials, such as insulating, semiconducting, superconducting or magnetic layers, in the heterostructure can fulfil different functionalities. Accordingly, we propose the use of a vdW semimetal as an active thermoelectric element for in-device cooling or for engineering a controllable temperature gradient within a device. A particularly promising vdW material for thermoelectric cooling is the Weyl semimetal WTe$_2$ because of its very high charge carrier mobility and near compensation of electron and hole densities[29–31]. In its bulk form, it has already been shown to display a large Nernst effect[32] and ultrahigh Ettingshausen effect at temperatures above 20 K (ref. 12).

Thermoelectric mechanisms in which out-of-equilibrium voltages or currents are generated by temperature gradients, like the Seebeck and Nernst effects, have been investigated extensively in microscopic vdW devices. These studies are typically performed by measuring voltages across microscopic contacts induced by global temperature gradients[21–26,33–35] or by local heating using, for example, a scanning focused laser beam[36–45]. In contrast, electro-thermal processes, like the Peltier and Ettingshausen effects, for which temperature gradients need to be measured or imaged in response to applied currents, are much more challenging to investigate in microscopic devices and have, thus far, been restricted to above liquid nitrogen temperatures[46,47]. In this work, we provide thermal imaging of magneto-electro-thermal cooling at liquid He temperatures in exfoliated flakes of the transition metal dichalcogenide WTe$_2$, revealing an ultrahigh Ettingshausen effect and the underlying mesoscopic mechanisms that have been inaccessible experimentally hitherto.

Cryogenic thermal imaging
A superconducting quantum interference device on a tip (SQUID-on-tip, SOT)[48] made of MoRe (ref. 49) with a diameter of 110 nm was scanned above the sample surface at a height $h \approx 80$ nm in an He exchange gas atmosphere. It was employed as a nanothermometer[50] with 2.6 μK Hz$^{-1/2}$ sensitivity at $T_0 = 4.3$ K, operating in an applied out-of-plane magnetic field of up to $B = 5$ T (Methods), as shown schematically in Fig. 1b. A high-quality WTe$_2$ single crystal[31] was exfoliated to produce a $d = 269$ nm thick flake and patterned by reactive ion etching (Methods) into a number of rectangular chambers with different widths W (Fig. 1c). To circumvent the $1/f$ noise of the SOT, a sine or square-wave a.c. current at frequency $f = 85.37$ Hz and variable rms amplitude I was applied to the three chambers, which were connected in series by narrow constrictions (Fig. 1c). The resulting a.c. change in the local temperature $\delta T(x,y)$ relative to the base temperature T_0 was imaged by the scanning SOT.

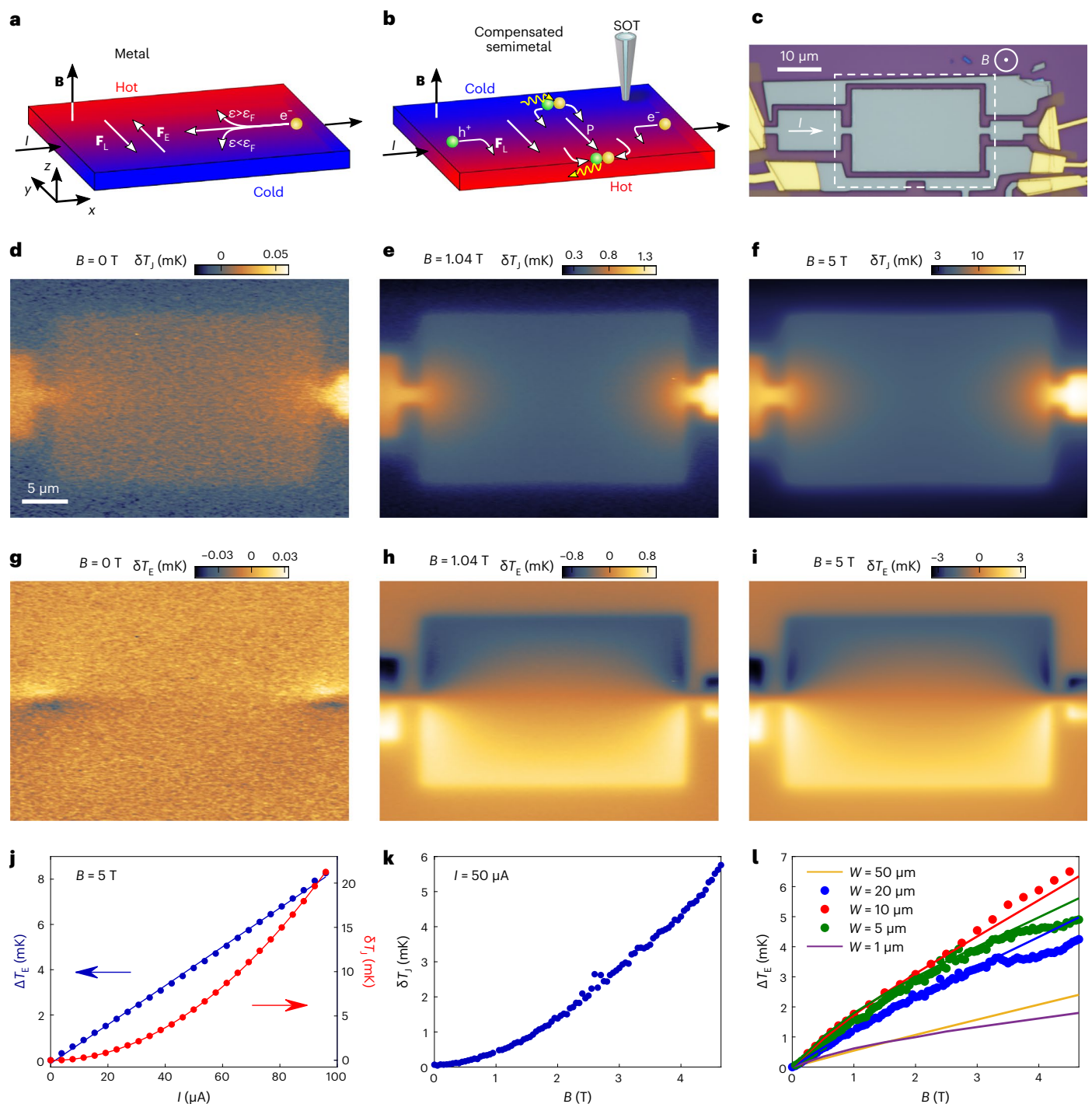## Imaging the Ettingshausen effect in WTe$_2$
The current-induced change in the local temperature δT has two contributions, one arising from Joule heating δT_J and the other from the Ettingshausen effect δT_E. By applying a sine-wave a.c. current through the sample, we can image these two contributions independently as follows. Since the Ettingshausen effect is linear in I, δT_E is a sine-wave temperature modulation at the frequency f of the applied current. We, thus, detect this contribution by lock-in measurement at the fundamental frequency f. In contrast, Joule heating is quadratic in I and, therefore, results in d.c. heating superimposed by an a.c. temperature modulation at frequency $2f$ (Methods). We image this a.c. δT_J modulation by lock-in detection at the second harmonic.

Figure 1d–f shows the Joule heating $\delta T_J(x,y)$ induced in the largest chamber (dashed rectangle in Fig. 1c) at $B = 0$, 1.04 and 5 T, respectively, at $I = 50$ μA (thermal images of the two smaller chambers of the device are shown in Extended Data Fig. 3). δT_J was rather uniform in most of the chamber area with intense hot spots at the constrictions where the current density is high. Figure 1j shows that δT_J in the chamber grew quadratically with I, as expected for Joule heating. δT_J increased by over two orders of magnitude with the field, growing approximately quadratically with B, as shown in Fig. 1k. This is the consequence of the very large magnetoresistance $\rho_{xx}(B) \propto B^2$ in high-purity WTe$_2$, as reported previously[29–32,51].

The Ettingshausen temperature distribution $\delta T_{E(x,y)}$ is shown in Fig. 1g–i. At zero field, $\delta T_E = 0$ as expected (the weak signal in the constrictions is an artefact; Methods). Upon increasing the field, a large temperature gradient developed transverse to the current and magnetic field directions. The temperature difference $\Delta T_E = \delta T_E(0,-W/2) - \delta T_E(0,W/2)$ between the hot (bottom) and the cold (top) edges at $y = \mp W/2$ across the sample centre ($x = 0$) grew linearly with I (Fig. 1j), as expected for the Ettingshausen effect, $\Delta T_E = P_E IB/W$, where P_E is the Ettingshausen coefficient. For $B = 5$ T and $W = 20$ μm, we found an ultrahigh Ettingshausen signal $\Delta T_E/(JW) = 2.2 \times 10^{-5}$ K A^{-1} m (J is the current density) comparable to the previously reported bulk values[12] but at a much lower temperature. However, in contrast to the standard bulk behaviour, we found that ΔT_E is not linear in B, as shown in Fig. 1l. Even more surprisingly, investigating chambers with different widths revealed a non-monotonic W dependence, with the chamber with $W = 10$ μm showing a larger ΔT_E than those with $W = 20$ μm or $W = 5$ μm (Fig. 1l). Moreover, Fig. 1h,i shows a non-trivial spatial distribution of $\delta T_E(x,y)$ with enhanced heating and cooling signals on the left and right edges near the constrictions. These features were also observed in additional samples, as shown in Extended Data Figs. 2–4.
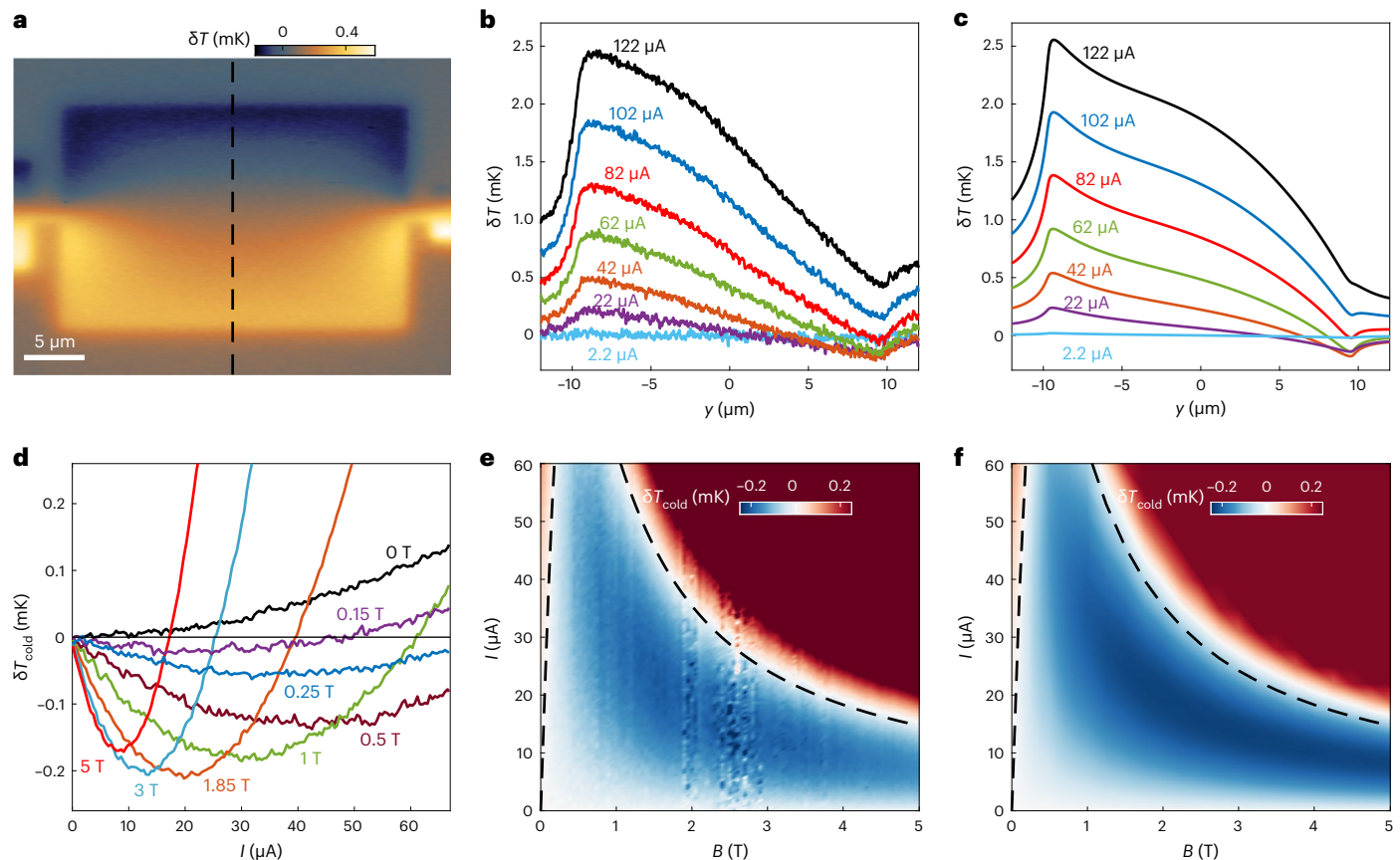
Absolute cooling
The linear increase of the Ettingshausen temperature difference ΔT_E with current does not necessarily mean that the temperature of the cold edge of the sample decreases monotonically with I or that real cooling has been achieved at the cold edge. This is because the Joule heating usually has a dominant contribution. The first and second harmonic a.c. temperature variations in response to a sine-wave a.c.

Fig. 1 | Thermal imaging of the Ettingshausen effect in a WTe₂ flake at 4.3 K.
a,b, Schematics of the Ettingshausen effect in metals (**a**) and in compensated semiconductors or semimetals (**b**) in the presence of a perpendicular magnetic field B. In a metal, the average Lorentz force $\mathbf{F_L}$ is counterbalanced by the transverse electrostatic force $\mathbf{F_E}$ of the Hall voltage. As the higher energy electrons usually have a lower drift velocity and, hence, lower $\mathbf{F_L}$, a small transverse thermoelectric effect develops. In semiconductors and semimetals, a much larger transverse temperature gradient of opposite sign is induced by electron–hole pair generation at the cold edge and recombination at the hot edge. **c**, Optical image of a WTe₂ device showing three rectangular chambers (grey) of widths of $W = 10$, 20 and 5 µm along with surrounding additional patterns. A sinusoidal a.c. current I at frequency f is applied in series (white arrow)

through the Au contacts (yellow). The dashed white rectangle marks the scan window in **d**–**i**. **d**–**f**, Temperature maps $\delta T_J(x,y)$ corresponding to Joule heating acquired at $2f$ with $I = 5$ µA at magnetic fields of $B = 0$ T (**d**), 1.04 T (**e**) and 5 T (**f**). **g**–**i**, Corresponding maps of Ettingshausen temperature component $\delta T_E(x,y)$ acquired simultaneously at f at magnetic fields of $B = 0$ T (**g**), 1.04 T (**h**) and 5 T (**i**). **j**, Left axis: temperature difference between the hot and cold edges ΔT_E (blue dots) versus I with a linear fit (blue line) at $B = 5$ T. Right axis: $\delta T_J(0,0)$ at the centre of the chamber versus I (red dots) and a parabolic fit (red line). **k**, Magnetic field dependence of δT_J at $I = 50$ µA. **l**, ΔT_E versus B in the three adjacent chambers of $W = 5$, 10 and 20 µm at $I = 50$ µA (dots) showing nonlinear dependence on B and non-monotonic dependence on W. The solid curves are the corresponding ΔT_E from the numerical simulations.

Fig. 2 | Absolute cooling. a, Map of the current-induced local excess temperature $\delta T(x,y)$ relative to the base temperature $T_0 = 4.3$ K, generated by a unipolar square-wave current excitation of $I = 25$ µA in the WTe$_2$ device at $B = 0.64$ T. Regions with negative δT are cooled by the current to below T_0. **b**, Profiles of excess temperature $\delta T(0, y)$ along the black dashed line in **a** at various applied currents. **c**, Simulated temperature profiles $\delta T(0, y)$. **d**, Excess temperature at the cold edge of the chamber δT_{cold} versus I at different magnetic fields showing absolute cooling $\delta T_{cold} < 0$. **e**, Measured $\delta T_{cold}(I, B)$ diagram showing the parameter space of absolute cooling (blue). **f**, Simulated $\delta T_{cold}(I, B)$ diagram. The colour in the high-temperature regions (red) in **e** and **f** is saturated for clarity. The dashed lines in **e** and **f** show the fit of the current $I_0(B)$ from equation (6) below which absolute cooling occurs.

current presented in Fig. 1 allowed us to distinguish between the Ettingshausen and Joule terms, but these terms do not include the d.c. Joule heating component (Methods). To map the actual map of excess temperature, we modulated the applied current between zero and I by applying a unipolar square wave. In this case, the measured a.c. $\delta T(x, y)$ provides an image of the total current-induced excess temperature, which is the difference between the local temperature $T(x, y) = T_0 + \delta T(x, y)$ in the presence of the current and the base temperature T_0 in its absence. Positive δT represents heating whereas negative δT is cooling to below T_0.

Figure 2a shows the resulting temperature map $\delta T(x, y)$ in the $W = 20$ µm chamber at $B = 0.64$ T and $I = 25$ µA. $\delta T(x, y)$ along the top edge of the sample is negative. That is, the local temperature in the presence of the current is below T_0, revealing current-induced absolute cooling. Even stronger cooling is observed in the top two corners of the chamber. To the best of our knowledge, this is the first observation of Ettingshausen cooling at liquid He temperatures.

Next, we explored the current and field dependence of the cooling mechanism. Figure 2b shows the temperature profile $\delta T(0, y)$ across the sample centre (dashed line in Fig. 2a) at $B = 0.64$ T and various applied currents I. The temperature at the hot edge ($y = -W/2$) increased monotonically with the current, and the temperature difference ΔT_E between the hot and cold edges increased linearly with I (Fig. 1j). Yet, the temperature at the cold edge ($y = W/2$) showed non-monotonic behaviour due to competition between the linear Ettingshausen cooling and the quadratic Joule heating. As a result, absolute cooling ($\delta T < 0$) was achieved only at low currents. Note that

at any current, the temperature at the cold edge was lower than the temperature at the hot edge or in the sample centre. That is, the relative Ettingshausen cooling always occurred, but at high currents it could not overcome the Joule heating to attain absolute cooling.

The cooling mechanism was also non-monotonic in magnetic field. Figure 2d shows $\delta T_{cold} = \delta T(0, W/2)$ versus I at different B. At $B = 0$, the excess temperature was always positive, increasing monotonically with I. At finite fields, δT_{cold} was negative at low currents, initially showing a negative slope with I, which increased monotonically with B. The current at which the maximal negative temperature $\delta T_{cold}^{max}(B)$ is attained decreased monotonically with B, but $\delta T_{cold}^{max}(B)$ has a non-monotonic B dependence with maximal negative δT_{cold}^{max} attained at $B \approx 2$ T. Figure 2e shows the full map of $\delta T_{cold}(B, I)$, revealing a wide range of fields and currents at which negative excess temperatures can be achieved (blue).

Theory of Ettingshausen effect in mesoscopic devices

The mechanism underlying the large Ettingshausen effect in WTe$_2$ stems from the near compensation of electron and hole densities, $n_e \approx n_h = n$, and their mobilities, $\mu_e \approx \mu_h = \mu$. In bulk devices, the induced transverse temperature difference $\Delta T_E = P_E IB/W$ is proportional to B/W (refs. 12,19,20). This relation does not hold in mesoscopic devices because of the competition between different microscopic length scales and due to the inherently non-uniform current distribution. Consider a bulk sample with uniform applied longitudinal

electric field $\mathbf{E} = E_x \hat{x}$. At $B = 0$ T, the resulting current density $\mathbf{J}$ comprises counterflowing particle flux densities of electrons $\mathbf{j}_e$ and holes $\mathbf{j}_h$, $\mathbf{J} = e(\mathbf{j}_h - \mathbf{j}_e)$, where e is the elementary charge. An out-of-plane magnetic field $\mathbf{B} = B\hat{z}$ gives rise to a transverse Lorentz force $\mathbf{F}_L$, which for a single-charge-type conductor is counterbalanced by the electrostatic force of the induced Hall voltage $\mathbf{F}_E$, resulting in the absence of magnetoresistance (Fig. 1a). In a compensated semimetal, in contrast, the Hall voltage vanishes and $\mathbf{F}_L$, which scales as μB, drives both the electrons and holes in the same transverse direction (Fig. 1b). This transverse flow of quasiparticles creates the quasiparticle current density $\mathbf{P} = e(\mathbf{j}_h + \mathbf{j}_e)$, which in turn causes a longitudinal Lorentz force that counteracts the force of the applied electric field, resulting in bulk magnetoresistance that scales as $(\mu B)^2$, $\rho_{xx} \cong \rho_0(1 + \mu^2 B^2)$, where ρ_0 is the zero-field resistivity[29–32,51].

The edges play a crucial role in a microscopic device. In particular, the boundary conditions preclude a transverse particle flow at the sample edges. This implies that the magnetoresistance, which is caused by the transverse flow, is suppressed near the boundaries. A recent theoretical study[52,53] showed that the resulting current distribution across the width $-W/2 \leq y \leq W/2$ of a long narrow strip is given by

$$J_x(y) = \frac{E_x}{\rho_0(1 + \mu^2 B^2)}\left[1 + \mu^2 B^2 \frac{\cosh(2y/l_R)}{\cosh(W/l_R)}\right], \quad (1)$$

where $l_R = l_R^0/\sqrt{1 + \mu^2 B^2}$ and l_R^0 is the electron–hole recombination length at zero field. For $l_R \ll W$, equation (1) shows that in the centre of the strip, the current density is suppressed by the magnetoresistance just like in the bulk limit, $J_x(|y| \ll W) = \frac{E_x}{\rho_0(1 + \mu^2 B^2)}$. Remarkably, along the edges, the current experiences no magnetoresistance, $J_x(|y| = W/2) = E_x/\rho_0$, remaining at its zero-field value. As a result, the current distribution peaks along the edges within narrow channels with a characteristic width of l_R (narrow bright slivers along the top and bottom edges in Fig. 3a).

In contrast to the conservation of charge current $\nabla \cdot \mathbf{J} = 0$, the quasiparticle current $\mathbf{P}$ is not conserved because electron–hole pairs can be generated and recombined. Hence $\nabla \cdot \mathbf{P} = -\delta n_q/\tau_R$, where $\delta n_q = \delta n_e + \delta n_h$ is the quasiparticle excess density, δn_e and δn_h are the out-of-equilibrium electron and hole densities, and τ_R is the electron–hole recombination time. In the narrow strip geometry, the resulting quasiparticle current and density distributions are given by

$$P_y(y) = -\frac{\mu B E_x}{\rho_0(1 + \mu^2 B^2)}\left[1 - \frac{\cosh(2y/l_R)}{\cosh(W/l_R)}\right]. \quad (2)$$

$$\delta n_q(y) = -\frac{2\mu B E_x}{\rho_0(1 + \mu^2 B^2)}\frac{\tau_R}{l_R}\frac{\sinh(2y/l_R)}{\cosh(W/l_R)}. \quad (3)$$

In the central part of the sample, δn_q is small because the quasiparticle thermal generation and recombination rates are approximately balanced, like in thermal equilibrium, and P_y is essentially constant, as shown in Fig. 3b,c. The transverse P_y driven by the Lorentz force gives rise to a sharp accumulation (depletion) of the quasiparticles within l_R from the bottom (top) edge. As a result, the electron–hole pair recombination rate is enhanced (suppressed) by $\delta n_q/\tau_R$ at the bottom (top) edge, giving rise to heating by phonon emission (cooling by phonon absorption).

The thermoelectric effect can, thus, be derived by considering the two heat-generating terms $\dot{Q} = \dot{Q}_J + \dot{Q}_E$, where $\dot{Q}_J = \mathbf{J} \cdot \mathbf{E}$ is the Joule term, $\dot{Q}_E = \epsilon_p \delta n_q/\tau_R = -\epsilon_p \nabla \cdot \mathbf{P}$ is the Ettingshausen contribution and ϵ_p is the average phonon energy released (absorbed) by recombination (generation) of an electron–hole pair:

$$\dot{Q}_J(y) = \frac{E_x^2}{\rho_0(1 + \mu^2 B^2)}\left[1 + \mu^2 B^2 \frac{\cosh(2y/l_R)}{\cosh(W/l_R)}\right], \quad (4)$$

$$\dot{Q}_E(y) = -\frac{2\epsilon_p \mu B E_x}{e \rho_0 l_R^0 \sqrt{1 + \mu^2 B^2}}\frac{\sinh(2y/l_R)}{\cosh(W/l_R)}. \quad (5)$$

As expected, $\dot{Q}_J$ is symmetric in y and quadratic in E_x and, hence, appears in the second harmonic for the a.c. current, whereas $\dot{Q}_E$ is antisymmetric in y and linear in E_x, consistent with the experimental results in Fig. 1.

To attain a better understanding of the thermoelectricity in mesoscopic systems, we ran three-dimensional (3D) finite-element numerical simulations for our sample geometry (Methods). Figure 3a shows that a high current density $\mathbf{J}$ is present in the constrictions, whereas in the rectangular chamber, the current density peaks along the sample edges where the magnetoresistance is suppressed. The corresponding Joule dissipation $\dot{Q}_J$ is highest in the constrictions (Fig. 3d) and is enhanced in the narrow slivers along the top and bottom edges in the chamber. The quasiparticle current density $\mathbf{P}(x, y)$ in Fig. 3b also shows a large enhancement in the constrictions. In the rectangular chamber, $\mathbf{P}$ flows mostly transverse to $\mathbf{J}$ and is largest in the central area. Note that $|\mathbf{P} \approx \mu B \mathbf{J}|$ is substantially larger than $|\mathbf{J}|$ for the presented case of $\mu B = 1.6$, which corresponds to our experimental values at $B = 0.64$ T. The excess quasiparticle density $\delta n_q(x, y)$ sharply peaks along the sample boundaries, including the left and right edges (Fig. 3c). As a result, the Ettingshausen dissipation $\dot{Q}_E$ (Fig. 3e) shows pronounced cooling along the edges in the top half of the sample and heating along the bottom-half edges. Depending on the parameters, the total dissipation $\dot{Q} = \dot{Q}_J + \dot{Q}_E$ can be either positive everywhere or negative (cooling) along the top boundaries, as shown in Fig. 3f.

By incorporating heat diffusion equations for WTe$_2$ and for the Si substrate into the numerical calculations (Methods), we can derive the corresponding δT_J, δT_E and the total δT distributions. Figure 3g–i shows that the calculated local temperatures follow the local $\dot{Q}$ maps in Fig. 3d–f, albeit broadened by the thermal heat conductivities in the flake and the substrate. In particular, the enhancement of $\dot{Q}_J$ in the narrow slivers along the edges in Fig. 3d is completely broadened in the δT_J map in Fig. 3g. We attain very good agreement between the numerical simulations and the experimental data for the microscopic parameters $l_R^0 = 0.5 \, \mu m$, $\mu = 25{,}000 \, cm^2 \, V^{-1} \, s^{-1}$ and $\epsilon_p = 0.06$ meV. The calculated temperature distributions shown in Fig. 3g–i match qualitatively very well the measured δT_J and δT_E maps in Fig. 1e,h and with the total δT distribution in Fig. 2a. Figure 2c shows the calculated $\delta T(y)$ profiles across the width of the sample at various currents, which reproduce well the experimental behaviour. Moreover, the experimental phase diagram of the absolute cooling $\delta T_{cold}(I, B)$ in Fig. 2e is also well described by the model (Fig. 2f), showing the accessible range of absolute cooling and the optimal parameters for achieving the lowest temperatures in our device. Finally, the model also recovers the non-monotonic width dependence and the nonlinearity of $\Delta T_E(B)$ in Fig. 1l (solid lines).

Analytical model

Further insight into the role of the different parameters in a mesoscopic device can be attained by considering a simplified model for the total heat fluxes. The lateral heat flux from the hot to the cold side of the device is governed by the in-plane total heat conductivity κ of WTe$_2$ with thickness d. Further, heat flows from the hot side of the device to the substrate and from the substrate to the cold part of the device. The flow of heat depends on the out-of-plane heat conductivity κ' of the substrate, which has effective thickness d_s. In this geometry, we find (Methods) that the condition on the applied current for attaining a negative excess temperature at the cold edge is $I < I_0$, where
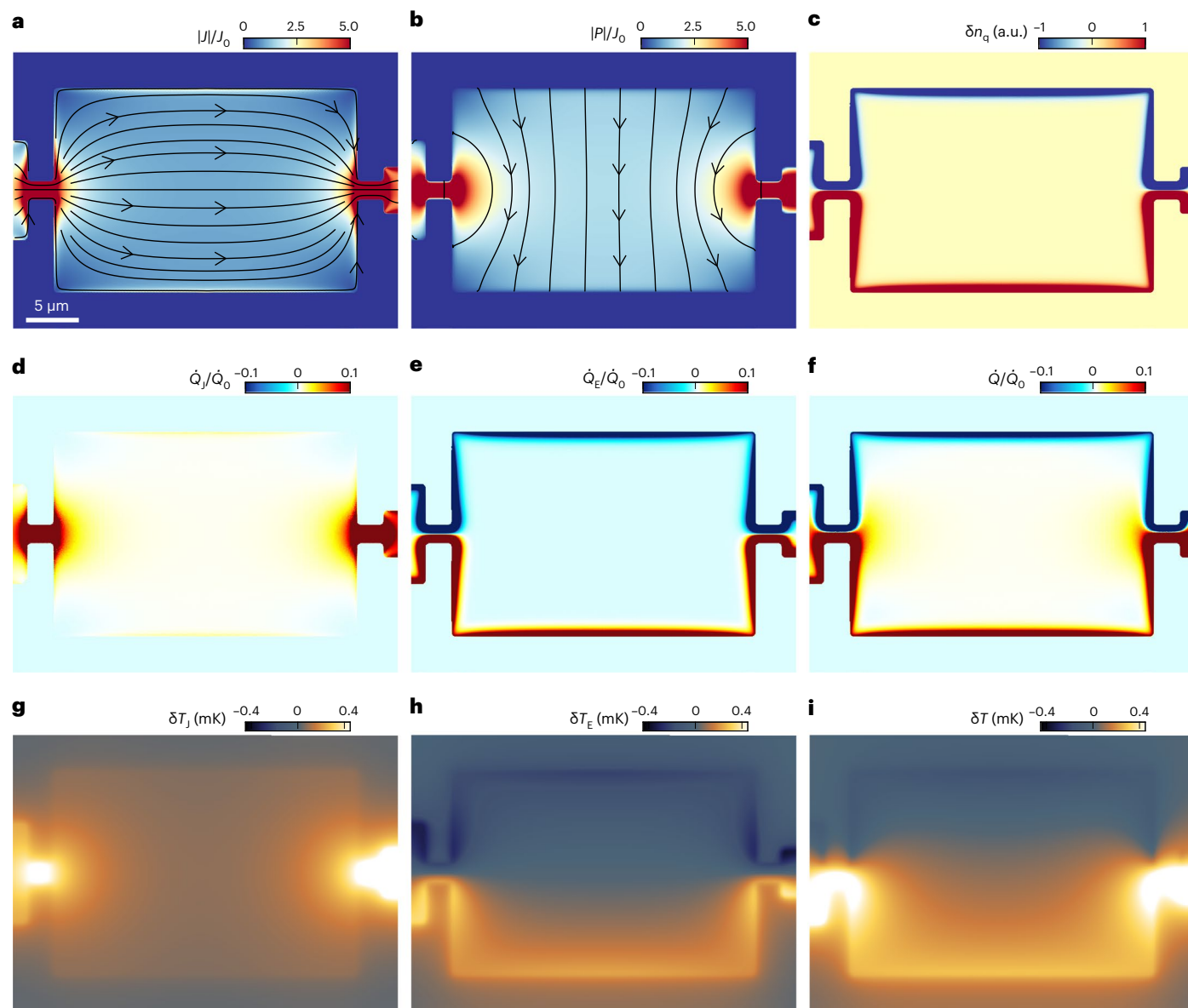
Fig. 3 | Numerical simulations of the magneto-thermoelectric response.
a, Normalized current density distribution $|\mathbf{J}(x,y)|$ and streamlines at $B = 0.64$ T and $I = 25\,\mu$A ($J_0 = I/W$). **b**, Quasiparticle current density $|\mathbf{P}(x,y)|$ with streamlines. **c**, Out-of-equilibrium quasiparticle density $\delta n_q(x,y)$. The colours are saturated for clarity. **d**, Power density generated by Joule heating $\dot{Q}_J(x,y)$. **e**, Power density

$\dot{Q}_E(x,y)$ produced by generation and recombination of quasiparticles due to the Ettingshausen effect. **f**, Total power density $\dot{Q} = \dot{Q}_J + \dot{Q}_E$. **g**, Excess temperature distribution δT_J caused by Joule heating. **h**, Excess temperature distribution δT_E caused by the Ettingshausen effect. **i**, Total excess temperature $\delta T(x,y)$. See Methods for simulation parameters.

$$I_0 \approx \frac{\epsilon_p}{e\rho_0} \frac{4\mu B}{\left(1 + \mu^2 B^2\right)\left(1 + W_0^2/W^2\right)} \qquad (6)$$

and $W_0 \approx \sqrt{8dd_s\kappa/\kappa'}$. The dashed curve in Fig. 2e shows that the fit of $I_0(B)$ to the experimental data provides a very good description of the cooling regime. Note that from equation (6), the maximum of $I_0(B)$ occurs at $\mu B = 1$, which allows a direct evaluation of $\mu \approx 23{,}000$ cm^2 V^{-1} s^{-1} from the experimental data, consistent with the more accurate 3D simulations, resulting in $\mu = 25{,}000$ cm^2 V^{-1} s^{-1}.

By integrating $\dot{Q}_E$ over the cold side of the sample and taking into account the above heat conductivities, we derive the transverse temperature difference (Methods):

$$\Delta T_E \approx \frac{\epsilon_p I}{ed\kappa} \frac{2\mu B}{\left(1 + \mu B l_R^0/W\right)\left(1 + W^2/W_0^2\right)}. \qquad (7)$$

This result emphasizes a number of key aspects of the mesoscopic nature of the Ettingshausen effect, which cannot be observed in bulk materials. The first is the sublinear dependence of ΔT_E on B due to the $\mu B l_R^0/W$ term, which allows us to evaluate the electron–hole recombination length $l_R^0 \approx 0.3\,\mu$m, which is close to the more accurate value derived numerically (Fig. 1l). In contrast, in the bulk limit of $W \gg \mu B l_R^0$, the common linear B dependence of ΔT_E is recovered, so that we are unable to determine l_R^0 from such measurements.

Second, equation (7) predicts a non-monotonic dependence of ΔT_E on W, which describes well the behaviour in Fig. 1l (see Extended Data Fig. 1 for more details). The largest ΔT_E should be attainable for $W \approx \sqrt[3]{W_0^2 l_R^0}\,\mu B$ for $\mu B < 1$. From our observation of the largest transverse temperature difference in the $W = 10\,\mu$m sample, we derive $W_0 \approx 24\,\mu$m. This new mesoscopic length scale W_0 arises due to the competition between the transverse heat conductivity across the

sample width and the heat conductivity to the substrate and is absent in the bulk case. This length scale can serve as an important parameter for further optimization of Ettingshausen cooling in microscopic devices.

Third, we derive that the largest cooling is attained at $\hat{I} = I_0/2$ and $\hat{B} = \frac{1}{\mu}\sqrt[3]{\frac{2W}{l_R^0}}$ (Methods) where the negative excess temperature reaches

$$\delta T_{cold}^{max} \approx -\frac{\epsilon_p^2}{e^2 \rho_0 d\kappa} \frac{W_0^2 W^2}{\left(W^2 + W_0^2\right)^2}. \tag{8}$$

For $W = 20\ \mu m$, this results in $\hat{B} \approx 2.2\ T$ and $\delta T_{cold}^{max} \approx -0.2\ mK$, in good agreement with Fig. 2d.

Equation (8) shows that lower cooling temperatures can be attained by reducing the sample sheet resistivity ρ_0. In our WTe$_2$ flake, $\rho_0 \approx 0.54\ \Omega$, corresponding to an effective bulk resistivity $\rho_0 d \approx 1.5 \times 10^{-5}\ \Omega\ cm$ ($d = 269\ nm$), which is almost two orders of magnitude higher than the low-temperature bulk resistivity $\rho \approx 2.3 \times 10^{-7}\ \Omega\ cm$ in high-quality crystals[31]. Since the increase in ρ_0 is attributed to surface oxidation[54], one can expect to attain substantially stronger cooling in devices fabricated in an inert environment and encapsulated in hBN.

Finally, from the combination of the derived parameters (Methods), we extracted the Ettingshausen conversion coefficient $\epsilon_p \approx 0.06\ meV$, which is about one sixth of the thermal energy of the quasiparticles ($k_B T_0 = 0.37\ meV$) and, thus, in good agreement with the description of the Ettingshausen effect in terms of particle–hole generation and recombination.

The developed nanoscale imaging of magneto-electro-thermal cooling at cryogenic temperatures in microscopic devices opens the door for studying and engineering thermal landscapes and energy harvesting in new electronic materials and devices. The derived microscopic model allows one to further enhance the cooling efficiency through the optimization of the electrical and thermal conductivity characteristics of the materials and of the device geometries. This study suggests the possibility of integrating transition metal dichalcogenide atomic layer semimetals in multilayer vdW heterostructures to provide for in-device electro-thermal cooling, temperature gradient engineering and studying thermoelectric effects in low-dimensional strongly correlated states of matter.

Online content

Any methods, additional references, Nature Portfolio reporting summaries, source data, extended data, supplementary information, acknowledgements, peer review information; details of author contributions and competing interests; and statements of data and code availability are available at https://doi.org/10.1038/s41567-024-02417-z.

References

1. Bell, L. E. Cooling, heating, generating power, and recovering waste heat with thermoelectric systems. *Science* **321**, 1457–1461 (2008).
2. Mao, J., Chen, G. & Ren, Z. Thermoelectric cooling materials. *Nat. Mater.* **20**, 454–461 (2021).
3. Li, P. et al. Colossal Nernst power factor in topological semimetal NbSb$_2$. *Nat. Commun.* **13**, 7612 (2022).
4. Watzman, S. J. et al. Dirac dispersion generates unusually large Nernst effect in Weyl semimetals. *Phys. Rev. B* **97**, 161404 (2018).
5. Han, F. et al. Quantized thermoelectric Hall effect induces giant power factor in a topological semimetal. *Nat. Commun.* **11**, 6167 (2020).
6. Wang, P. et al. Giant Nernst effect and field-enhanced transversal z_NT in ZrTe$_5$. *Phys. Rev. B* **103**, 45203 (2021).
7. Fu, C. et al. Largely suppressed magneto-thermal conductivity and enhanced magneto-thermoelectric properties in PtSn$_4$. *Research* **2020**, 4643507 (2020).
8. Fu, C. et al. Large Nernst power factor over a broad temperature range in polycrystalline Weyl semimetal NbP. *Energy Environ. Sci.* **11**, 2813–2820 (2018).
9. Liu, W. et al. Weyl semimetal states generated extraordinary quasi-linear magnetoresistance and Nernst thermoelectric power factor in polycrystalline NbP. *Adv. Funct. Mater.* **32**, 2202143 (2022).
10. Feng, T. et al. Large transverse and longitudinal magneto-thermoelectric effect in polycrystalline nodal-line semimetal Mg$_3$Bi$_2$. *Adv. Mater.* **34**, 2200931 (2022).
11. Chen, Z. et al. Leveraging bipolar effect to enhance transverse thermoelectricity in semimetal Mg$_2$Pb for cryogenic heat pumping. *Nat. Commun.* **12**, 3837 (2021).
12. Pan, Y. et al. Ultrahigh transverse thermoelectric power factor in flexible Weyl semimetal WTe$_2$. *Nat. Commun.* **13**, 3909 (2022).
13. DiSalvo, F. J. Thermoelectric cooling and power generation. *Science* **285**, 703–706 (1999).
14. Sidorenko, N., Parashchuk, T., Maksymuk, M. & Dashevsky, Z. Development of cryogenic cooler based on n-type Bi–Sb thermoelectric and HTSC. *Cryogenics* **112**, 103197 (2020).
15. Harutyunyan, S. R. et al. Thermoelectric cooling at cryogenic temperatures. *Appl. Phys. Lett.* **83**, 2142–2144 (2003).
16. Giazotto, F., Heikkilä, T. T., Luukanen, A., Savin, A. M. & Pekola, J. P. Opportunities for mesoscopics in thermometry and refrigeration: physics and applications. *Rev. Mod. Phys.* **78**, 217–274 (2006).
17. Muhonen, J. T., Meschke, M. & Pekola, J. P. Micrometre-scale refrigerators. *Rep. Prog. Phys.* **75**, 046501 (2012).
18. Ziabari, A., Zebarjadi, M., Vashaee, D. & Shakouri, A. Nanoscale solid-state cooling: a review. *Rep. Prog. Phys.* **79**, 095901 (2016).
19. Paranjape, B. V. & Levinger, J. S. Theory of the Ettingshausen effect in semiconductors. *Phys. Rev.* **120**, 437–441 (1960).
20. Delves, R. T. The prospects for Ettingshausen and Peltier cooling at low temperatures. *Br. J. Appl. Phys.* **13**, 440–445 (1962).
21. Zuev, Y. M., Chang, W. & Kim, P. Thermoelectric and magnetothermoelectric transport measurements of graphene. *Phys. Rev. Lett.* **102**, 096807 (2009).
22. Checkelsky, J. G. & Ong, N. P. Thermopower and Nernst effect in graphene in a magnetic field. *Phys. Rev. B* **80**, 081413 (2009).
23. Duan, J. et al. High thermoelectricpower factor in graphene/hBN devices. *Proc. Natl Acad. Sci. USA* **113**, 14272–14276 (2016).
24. Ghawri, B. et al. Breakdown of semiclassical description of thermoelectricity in near-magic angle twisted bilayer graphene. *Nat. Commun.* **13**, 1522 (2022).
25. Paul, A. K. et al. Interaction-driven giant thermopower in magic-angle twisted bilayer graphene. *Nat. Phys.* **18**, 691–698 (2022).
26. Bhowmik, S. et al. Broken-symmetry states at half-integer band fillings in twisted bilayer graphene. *Nat. Phys.* **18**, 639–643 (2022).
27. Geim, A. K. & Grigorieva, I. V. Van der Waals heterostructures. *Nature* **499**, 419–425 (2013).
28. Andrei, E. Y. et al. The marvels of moiré materials. *Nat. Rev. Mater.* **6**, 201–206 (2021).
29. Ali, M. N. et al. Large, non-saturating magnetoresistance in WTe$_2$. *Nature* **514**, 205–208 (2014).
30. Wang, L. et al. Tuning magnetotransport in a compensated semimetal at the atomic scale. *Nat. Commun.* **6**, 8892 (2015).
31. Aharon-Steinberg, A. et al. Direct observation of vortices in an electron fluid. *Nature* **607**, 74–80 (2022).
32. Zhu, Z. et al. Quantum oscillations, thermoelectric coefficients, and the Fermi surface of semimetallic WTe$_2$. *Phys. Rev. Lett.* **114**, 176601 (2015).

33. Nam, S.-G., Ki, D.-K. & Lee, H.-J. Thermoelectric transport of massive Dirac fermions in bilayer graphene. *Phys. Rev. B* **82**, 245416 (2010).

34. Wang, C.-R. et al. Enhanced thermoelectric power in dual-gated bilayer graphene. *Phys. Rev. Lett.* **107**, 186602 (2011).

35. Ghahari, F. et al. Enhanced thermoelectric power in graphene: violation of the Mott relation by inelastic scattering. *Phys. Rev. Lett.* **116**, 136802 (2016).

36. Xu, X., Gabor, N. M., Alden, J. S., van der Zande, A. M. & McEuen, P. L. Photo-thermoelectric effect at a graphene interface junction. *Nano Lett.* **10**, 562–566 (2010).

37. Gabor, N. M. et al. Hot carrier-assisted intrinsic photoresponse in graphene. *Science* **334**, 648–652 (2011).

38. Buscema, M. et al. Large and tunable photothermoelectric effect in single-layer MoS_2. *Nano Lett.* **13**, 358–363 (2013).

39. Wu, S. et al. Multiple hot-carrier collection in photo-excited graphene moiré superlattices. *Sci. Adv.* **2**, e1600002 (2016).

40. Cao, H. et al. Photo-Nernst current in graphene. *Nat. Phys.* **12**, 236–239 (2016).

41. Lundeberg, M. B. et al. Thermoelectric detection and imaging of propagating graphene plasmons. *Nat. Mater.* **16**, 204–207 (2017).

42. Shautsova, V. et al. Plasmon induced thermoelectric effect in graphene. *Nat. Commun.* **9**, 5190 (2018).

43. Harzheim, A., Evangeli, C., Kolosov, O. V. & Gehring, P. Direct mapping of local Seebeck coefficient in 2D material nanostructures via scanning thermal gate microscopy. *2D Mater.* **7**, 041004 (2020).

44. Hesp, N. C. H. et al. Nano-imaging photoresponse in a moiré unit cell of minimally twisted bilayer graphene. *Nat. Commun.* **12**, 1640 (2021).

45. Razeghi, M. et al. Single-material MoS_2 thermoelectric junction enabled by substrate engineering. *npj 2D Mater. Appl.* **7**, 36 (2023).

46. Grosse, K. L., Bae, M.-H., Lian, F., Pop, E. & King, W. P. Nanoscale Joule heating, Peltier cooling and current crowding at graphene–metal contacts. *Nat. Nanotechnol.* **6**, 287–290 (2011).

47. Vera-Marun, I. J., van den Berg, J. J., Dejene, F. K. & van Wees, B. J. Direct electronic measurement of Peltier cooling and heating in graphene. *Nat. Commun.* **7**, 11525 (2016).

48. Vasyukov, D. et al. A scanning superconducting quantum interference device with single electron spin sensitivity. *Nat. Nanotechnol.* **8**, 639–644 (2013).

49. Bagani, K. et al. Sputtered $Mo_{66}Re_{34}$ SQUID-on-tip for high-field magnetic and thermal nanoimaging. *Phys. Rev. Appl.* **12**, 044062 (2019).

50. Halbertal, D. et al. Nanoscale thermal imaging of dissipation in quantum systems. *Nature* **539**, 407–410 (2016).

51. Ali, M. N. et al. Correlation of crystal quality and extreme magnetoresistance of WTe_2. *Europhys. Lett.* **110**, 67002 (2015).

52. Alekseev, P. S. et al. Magnetoresistance in two-component systems. *Phys. Rev. Lett.* **114**, 156601 (2015).

53. Alekseev, P. S. et al. Magnetoresistance of compensated semimetals in confined geometries. *Phys. Rev. B* **95**, 165410 (2017).

54. Woods, J. M. et al. Suppression of magnetoresistance in thin WTe_2 flakes by surface oxidation. *ACS Appl. Mater. Interfaces* **9**, 23175–23180 (2017).

Methods

WTe₂ device fabrication

High-quality WTe₂ single crystals were grown using a flux growth technique[51] as described in ref. [31]. Bulk samples produced by this method showed a residual resistance ratio of 3,250, a magnetoresistance ratio of up to 62,000 at 9 T and 2 K, and a mean free path $l_{mr} \approx 20\ \mu m$ (ref. [31]). The crystals were then used to mechanically exfoliate WTe₂ flakes onto oxidized silicon wafers (290 nm of SiO₂). Suitable flakes, identified by optical and atomic force microscopy, were then processed by electron-beam lithography and inductively coupled plasma etching into the various geometries. The latter was done with a flow of 20 sccm of SF₆ and 10 sccm of O₂ at a radio-frequency power of 25 W, which provides an etching rate of WTe₂ of about 4.7 nm min⁻¹. Electrical contacts were fabricated by an additional electron-beam lithography step, Ar ion milling to remove the native oxide layer of WTe₂, followed by electron-beam deposition of 3 nm of Ti and Au to a thickness that exceeded the WTe₂ flake thickness. Transport measurements of the flakes show carrier mobilities of about 10,000 to 30,000 cm² V⁻¹ s⁻¹ at 4 K, corresponding to a mean free path of $l_{mr} \approx 0.7$ to 2 µm, more than an order of magnitude lower than the bulk values due to surface oxidation and scattering, as reported previously[31,54].

SOT fabrication and thermal imaging

Nanoscale SOTs have been used as high-precision local thermometers to study dissipation in mesoscopic systems[50,55–57]. This is achieved through the strong dependence of the SOT critical current $I_c(T)$ on the SOT temperature. In practice, the SOT is connected in parallel with a small shunt resistor and biased above the critical current, $I_{bias} > I_c$. As a result, the current through the SOT $I_{SOT}(T)$ has a temperature dependence that approximately follows $I_c(T)$, with the best sensitivity in the temperature range $T_c/2 < T < T_c$. The thermal coupling between the SOT and the sample was achieved with a low-pressure He exchange gas. A cryogenic SQUID series array amplifier[58] was used for the I_{SOT} readout.

SOTs with a diameter around 110 nm were fabricated as described in refs. [48,59]. In this work, MoRe ($T_c \approx 7.2\ K$) was used as the superconducting material for the SOT to provide thermal sensitivity throughout the magnetic field range up to 5 T (ref. [49]) with a thermal sensitivity at zero field of 2.6 µK Hz⁻¹ᐟ². Calibrating the temperature sensitivity of the SOT at zero field was carried out using a heater installed in the microscope. The relative magnetic field dependence of the sensitivity was derived by imaging the temperature of an Au thin-film heater, which was patterned next to the WTe₂ flake, versus B. The MoRe SOT was intentionally chosen to have a weak sensitivity to a magnetic field that decreased rapidly with the magnetic field[49]. All data presented were acquired when the magnetic signal due to the Oersted field of the current flowing in the sample was negligible compared with the thermal signal, except for Fig. 1g, where a small signal at zero field can be resolved in the constrictions.

The SOT height was controlled by attaching the tip to a quartz tuning fork[50], which allowed scanning at a height of 80 nm above the sample surface. Thermal imaging was done at a base temperature of 4.3 K and in an environment of 40 mbar of He exchange gas to provide the thermal link between the tip and the sample[50]. All images in the main text were acquired with image resolution of 344 × 269 pixels, a pixel size of 90 nm and an acquisition time of 40 ms per pixel.

For the scans in Fig. 1, an a.c. bipolar sine wave with an rms current of $I = 50\ \mu A$ and an excitation frequency of $f = 85.37\ Hz$ was applied, and the resulting thermal response of the SOT was measured at the first and second harmonics of f using a lock-in amplifier. Note that a current $I(t) = I_0 \cos(\omega t)$ creates Joule heating $\dot{Q}_J(t) = RI^2(t) = \frac{1}{2}RI_0^2 + \frac{1}{2}RI_0^2 \cos(2\omega t)$, which has a d.c. component and a superimposed a.c. component at twice the excitation frequency. The latter a.c. component was measured by the second harmonic signal of the SOT.

To capture the total current-induced local temperature change in the sample δT relative to the base temperature T_0, we applied a unipolar square-wave excitation and measured the difference between the current-on and the current-off states, as presented in Fig. 2a. Negative δT means absolute current-induced cooling. That is, in the current-on state, the local temperature is lower than in the current-off state.

Analytical derivation of the Ettingshausen effect

Here we describe the simplified heat flux model. The results are in good agreement with the full numerical simulations and provide deeper insights into the role of the different parameters. We assume an approximately linear temperature gradient across the width $-W/2 \leq y \leq W/2$ of the sample, $T(y) = T_0 - |\delta T_{cold}| + (0.5 + y/W)\Delta T_E$, and calculate the lateral and out-of-plane heat fluxes. The lateral heat flux through the flake from the hot to the cold side of the device is $q_0 = d\kappa \Delta T_E/W$. We compare the heat fluxes into and out of the substrate by separately considering the two regions of the sample $-W/2 \leq y \leq 0$ and $0 < y \leq W/2$. By integrating over each region, we attain the heat flux from the hotter part of the sample into the substrate:

$$q_h = \frac{\kappa'}{d_s} \int_0^{W/2} (T(y) - T_0)\,dy = W\kappa'(3\Delta T_E - 4|\delta T_{cold}|)/8d_s.$$

Similarly, the heat flux from the substrate into the colder side:

$$q_c = \frac{\kappa'}{d_s} \int_{-W/2}^0 (T_0 - T(y))\,dy = W\kappa'(4|\delta T_{cold}| - \Delta T_E)/8d_s.$$

This leads to $q_h + q_c = W\kappa'\Delta T_E/4d_s$ and $q_h - q_c = W\kappa'(\Delta T_E - 2|\delta T_{cold}|)/2d_s$. The total heat flow generated by the Ettingshausen heating is, thus, described by

$$2\int_{-W/2}^0 \dot{Q}_E\,dy \approx 2q_0 + q_h + q_c = \left(\frac{2d\kappa}{W} + \frac{W\kappa'}{4d_s}\right)\Delta T_E. \tag{9}$$

The heat flow due to Joule heating in the same area is given by:

$$2\int_{-W/2}^0 \dot{Q}_J\,dy = q_h - q_c = \frac{W\kappa'}{2d_s}\left(\Delta T_E - 2|\delta T_{cold}|\right). \tag{10}$$

Introducing the length scale $W_0 = \sqrt{8dd_s\kappa/\kappa'}$ and solving for $|\delta T_{cold}|$ and the temperature difference ΔT_E, thus results in

$$\Delta T_E = \frac{\epsilon_p I}{ed\kappa}\frac{2\mu B}{(1 + \mu B l_R^0/W)(1 + W^2/W_0^2)}, \tag{11}$$

$$|\delta T_{cold}| = \frac{\frac{\rho_0 I^2}{4}(1 + \mu^2 B^2) - I\frac{\epsilon_p}{e}\frac{\mu B}{1 + W_0^2/W^2}}{d\kappa\frac{W^2}{W_0^2}\left(1 + \frac{\mu^2 B^2}{\sqrt{1 + \mu^2 B^2}}\frac{l_R^0}{W}\right)}. \tag{12}$$

The current at which the Joule heating at the cold edge balances the Ettingshausen cooling, resulting in $|\delta T_{cold}| = 0$, is thus given by

$$I_0 \approx \frac{\epsilon_p}{e\rho_0}\frac{4\mu B}{(1 + \mu^2 B^2)\left(1 + \frac{W_0^2}{W^2}\right)}. \tag{13}$$

The maximal cooling is attained at $\hat{I} = I_0/2$ and $\hat{B} = \frac{1}{\mu}\sqrt[3]{\frac{2W}{l_R^0}}$, with the lowest temperature of

$$\delta T_{cold}^{max}(\hat{B}) \approx -\frac{\epsilon_p^2}{e^2\rho_0 d\kappa}\frac{W_0^2 W^2}{(W^2 + W_0^2)^2}. \tag{14}$$

The fit to the experimental data is performed in three steps. The values of μ and the combined coefficient $C_1 = \frac{\epsilon_p}{e\rho_0}\frac{1}{(1 + W_0^2/W^2)}$ can be

determined from fitting the line $|\delta T_{cold}| = 0$ in the phase diagram in Fig. 2e. Subsequently, the non-monotonic dependence of ΔT_E as a function of W for a given current I in equation (11) can be used to yield estimates for W_0, l_R^0 and the global coefficient $C_2 = \frac{\epsilon_p}{ed\kappa}$, as shown in Extended Data Fig. 1a,b. These values can then be used to evaluate $\delta T_{cold}^{max} = -C_1 C_2 \frac{W_0^2}{(W^2 + W_0^2)}$ (Extended Data Fig. 1c). Finally, from C_1 and using the zero-field sheet resistance $\rho_0 \approx 0.54\,\Omega$ derived from the full numerical fits, we can evaluate $\epsilon_p \approx 0.06$ meV.

Figure 2e,f and Extended Data Fig. 1 show that the analytical derivation captures well the essence of the Ettingshausen effect and of the absolute cooling in mesoscopic devices, although it considers a simplified model compared with the numerical simulations presented in Figs. 1l and 2f. The fitted values of μ and l_R^0 are slightly different between the analytical fits and the numerical simulations.

Numerical simulations

Finite-element 3D numerical simulations of the temperature maps due to Joule heating and the Ettingshausen effect in a nearly compensated semimetal were used to fit the experimental data. The calculations were conducted using COMSOL Multiphysics 5.4 in two consecutive steps. In the first step, the transport equations of a two-component conductor[53] were solved:

$$\frac{l_R^2}{\tau_R} \nabla \delta n_\alpha - n_\alpha \mu_\alpha \mathbf{E} - \mathbf{j}_\alpha \times (\mu_\alpha \mathbf{B}) = -\mathbf{j}_\alpha \tag{15a}$$

$$\text{div}\,\mathbf{j}_{e(h)} = -\frac{\delta n_q}{2\tau_R}, \tag{15b}$$

where the index α = e or h describes electrons or holes, $\mathbf{j}_\alpha$ are the particle flux densities, $\mathbf{E} = -\nabla\phi$ is the electric field, ϕ is the electric potential, n_e and n_h are the equilibrium densities of electrons and holes, $\delta n_q = \delta n_e + \delta n_h$ is the total out-of-equilibrium quasiparticle density, $\mu_{e(h)}$ is the electron (hole) mobility, τ_R is the characteristic recombination time and l_R is the recombination length. The recombination length and time are related by $l_R = \sqrt{D\tau_R}$, where D is the diffusion coefficient. To represent these equations, we used the Coefficients Form PDE module, which solves the general equation:

$$e_a \frac{\partial^2 \mathbf{u}}{\partial t^2} + d_a \frac{\partial \mathbf{u}}{\partial t} + \nabla \cdot (-c\nabla\mathbf{u} - \alpha\mathbf{u} + \gamma) + \beta \cdot \nabla\mathbf{u} + a\mathbf{u} = f, \tag{16}$$

where the field $\mathbf{u}$ is

$$\mathbf{u} = \left(\tilde{\phi} \ \widetilde{\delta n_q} \ ej_{e,x} \ ej_{e,y} \ ej_{h,x} \ ej_{h,y} \right). \tag{17}$$

Here $\tilde{\phi} = \left(\frac{e^2}{h}\right)\frac{1}{ld}\phi$, $\widetilde{\delta n_q} = (l_R/\tau_R)\,e\delta n_q$ and $l = 1\,\mu m$ is a length scale for expressing $\mathbf{u}$ in units of current density. Equation (16) was solved in a 3D geometry that follows the dimensions of the experimental sample depicted in Fig. 1c, using fitted parameters $\mu_e = \mu_h = 25{,}000\,cm^2\,V^{-1}\,s^{-1}$, $n_e = n_h = 2.1 \times 10^{18}\,cm^{-3}$ and $l_R^0 = 0.5\,\mu m$.

The heat transport was solved in the second step of the simulation. For this, we employed a heat transfer in solids module to simulate heat diffusion in the system. The 3D geometry consisted of the WTe$_2$ sample of thickness $d = 269$ nm, heat conductivity of $\kappa_{WTe_2} = 6.4\,W\,K^{-1}\,m^{-1}$, a He exchange gas layer surrounding the sample that extends 1 μm above it ($\kappa_{He} = 0.005\,W\,K^{-1}\,m^{-1}$), a SiO$_2$ layer of thickness 300 nm ($\kappa_{SiO_2} = 0.2\,W\,K^{-1}\,m^{-1}$), and a Si layer of thickness 5 μm ($\kappa_{Si} = 0.32\,W\,K^{-1}\,m^{-1}$), which was applied for practical convenience. From the solution of equation (16) in the first step, we calculated $\dot{Q}_E = \epsilon_p \delta n_q/\tau_R$, $\dot{Q}_J = -\mathbf{J} \cdot \nabla\phi$, and $\dot{Q} = \dot{Q}_J + \dot{Q}_E$ with $\epsilon_p = 0.16 k_b T_0 = 0.06$ meV, and used these as the heat sources for the heat transfer module to solve

for δT_E, δT_J and δT. The bottom side of the Si layer was set as the thermal anchor to $T_0 = 4.3$ K.

Note that although l_R^0 and μ affect the fitting to the experimental data substantially, the rest of the parameters provide a fit over a range of values. The simulations presented should, thus, be considered as a qualitative demonstration of the validity of the model rather than an accurate determination of the parameter values.

Ettingshausen effect in additional samples

Strip geometry. To exclude excess heating arising from the narrow constrictions in the rectangular chamber geometry, a sample with a strip geometry (Extended Data Fig. 2a) of width $W = 20\,\mu m$ and thickness $d = 160$ nm was investigated. By applying a sinusoidal a.c. current with $I = 50\,\mu A$ at $B = 5$ T, we acquired the maps of δT_J and δT_E shown in Extended Data Fig. 2d,e. The absence of the constrictions resulted in more uniform temperature distributions in the device compared with Fig. 1f,i. The slight canting of the thermal distributions in Extended Data Fig. 2d,e is probably due to the small Hall voltage resulting from incomplete compensation between the electron and hole densities and mobilities and shows an opposite tilt angle upon reversing the magnetic field direction (Supplementary Information). A quantitative analysis of the field dependence of δT_J at the centre of the device (Extended Data Fig. 2b) shows quadratic behaviour that approximately follows the B dependence of the sample resistivity, whereas the temperature difference $\Delta T_E = \delta T_E(0, -W/2) - \delta T_E(0, W/2)$ between the hot and cold edges across the centre of the strip shows an approximately linear B dependence consistent with Fig. 1k,l.

Applying a unipolar square-wave excitation with $I = 8\,\mu A$ at $B = 5$ T reveals absolute cooling at the top edge in Extended Data Fig. 2f. The phase space for absolute cooling was found by mapping δT_{cold} versus B and I, as shown in Extended Data Fig. 2c. The overall behaviour is like the $W = 20\,\mu m$ device in Fig. 2e with comparable δT_{cold} values. The main two quantitative differences, however, are the position of the peak of $I_0(B)$, which occurs at $B \approx 1.1$ T in Extended Data Fig. 2c, and the maximal negative δT_{cold}^{max} attained at $B \gtrsim 5$ T. By fitting the $I_0(B)$ (dashed line in Extended Data Fig. 2c), we find $\mu = 9{,}000\,cm^2\,V^{-1}\,s^{-1}$. This lower value is consistent with this device being thinner[31,54].

Rectangular geometry. We present here thermal imaging of an additional two chambers of width $W = 10$ and $5\,\mu m$ connected in series with the $W = 20\,\mu m$ chamber described in the main text (Fig. 1c). Extended Data Fig. 3a–c shows δT_J maps at $B = 0$, 1 and 5 T in the $W = 10\,\mu m$ chamber at $I = 50\,\mu A$ with corresponding δT_E maps in Extended Data Fig. 3d–f. A similar set of data is presented in Extended Data Fig. 3g–l for the $W = 5\,\mu m$ chamber. The qualitative behaviour is like that of the $W = 20\,\mu m$ chamber. However, ΔT_E shows a non-monotonic dependence on W, as described in Fig. 1l.

Additional geometries. Additional samples with more complex geometries are presented in Extended Data Fig. 4. Since an accurate calibration of the SOT thermal response was not available in this set of experiments, the data are presented in relative units.

Extended Data Fig. 4a,d shows a sample with thickness $d = 110$ nm, which allows the application of current through channels of different widths and along different directions. For the current path shown in Extended Data Fig. 4a, the largest δT_J was observed in Extended Data Fig. 4b in the two narrowest channels on the left and right sides. In contrast, the largest transverse ΔT_E occurs in the widest top left channel in Extended Data Fig. 4c. Additionally, strongly non-local Ettingshausen heating and cooling can be observed in the vicinity of the right-angled corners along the current path, as discussed below.

Application of the current along the central vertical channel in Extended Data Fig. 4d reveals that ΔT_E in the vertical strip sections in Extended Data Fig. 4f is smaller than the Ettingshausen heating and cooling spots appearing at the junctions with the horizontal channels.

The temperature maps for the two different current paths in the sample illustrate the mesoscopic nature of the Ettingshausen effect, as discussed in the main text, along with its non-local character. The Joule heating is local in nature because $\dot{Q}_J$ is mainly determined by the local J. In contrast, $\dot{Q}_E$ is not determined by the local P but rather by $\nabla \cdot \mathbf{P}$.

These features were further corroborated by thermal imaging of the sample shown in Extended Data Fig. 4g, which has thickness $d = 48$ nm and was used in ref. 31. This sample consists of a very narrow strip of $W = 0.55$ μm connected to two circular discs of 1.8 μm diameter. Extended Data Fig. 4h,i shows that δT_J is largest along the narrow horizontal strip, whereas ΔT_E is vanishingly small. In narrow channels, with width comparable to l_R, the regions of electron–hole generation and recombination partially overlap and the induced Ettingshausen temperature gradient is greatly suppressed by the large transverse heat conductivity across the narrow channel. In sharp contrast, Extended Data Fig. 4i shows very pronounced Ettingshausen heating and cooling in the circular chambers, where almost no current flows, emphasizing its non-local character.

Qualitatively, the dependence of δT_E on the channel width can also be seen in the temperature maps of the sample depicted in Extended Data Fig. 4j,m, which has two connected channels of different widths and a thickness of $d = 105$ nm. As seen in Extended Data Fig. 4l, the temperature difference between the hot and cold edges ΔT_E is larger in the wider channel and there is a pronounced increase in Ettingshausen heating and cooling at the corners, like the results in the main text (Fig. 1h,i). As expected for the Ettingshausen effect, δT_E reverses sign upon reversing the magnetic field direction in Extended Data Fig. 4o, whereas the Joule heating shown in Extended Data Fig. 4k,n remains unaffected.

Data availability
The data that support the findings of this study are available from the corresponding author on reasonable request.

Code availability
The finite-element COMSOL numerical simulation codes are available from the corresponding author on reasonable request.

References

55. Halbertal, D. et al. Imaging resonant dissipation from individual atomic defects in graphene. *Science* **358**, 1303–1306 (2017).
56. Marguerite, A. et al. Imaging work and dissipation in the quantum Hall state in graphene. *Nature* **575**, 628–633 (2019).
57. Aharon-Steinberg, A. et al. Long-range nontopological edge currents in charge-neutral graphene. *Nature* **593**, 528–534 (2021).
58. Huber, M. E. et al. DC SQUID series array amplifiers with 120 MHz bandwidth. *IEEE Trans. Appl. Supercond.* **11**, 1251–1256 (2001).
59. Finkler, A. et al. Self-aligned nanoscale SQUID on a tip. *Nano Lett.* **10**, 1046–1049 (2010).

Author contributions
T.V. and A.A.-S. performed the cryogenic thermal imaging measurements. A.K.P. and M.H. grew and characterized the WTe$_2$ crystals. E.A. designed and fabricated the samples. N.B. fabricated the SOT, and Y.M. developed the tuning fork feedback. M.E.H. designed and built the SOT readout system. A.A.-S. performed the finite-element COMSOL numerical simulations. T.H. and A.A.-S. developed the analytical derivation of the Ettingshausen effect. T.V., A.A.-S. and E.A. analysed the data. T.V., E.Z., A.A.-S. and T.H. wrote the original paper. All authors were involved in editing and reviewing the paper.

Competing interests
The authors declare no competing interests.

Additional information
**Extended data** Extended data are available for this paper at https://doi.org/10.1038/s41567-024-02417-z.

Supplementary information The online version contains supplementary material available at https://doi.org/10.1038/s41567-024-02417-z.

Correspondence and requests for materials should be addressed to E. Zeldov.

Peer review information *Nature Physics* thanks Ilari Maasilta and Ivan Vera-Marun for their contribution to the peer review of this work.

**Reprints and permissions information** is available at www.nature.com/reprints.
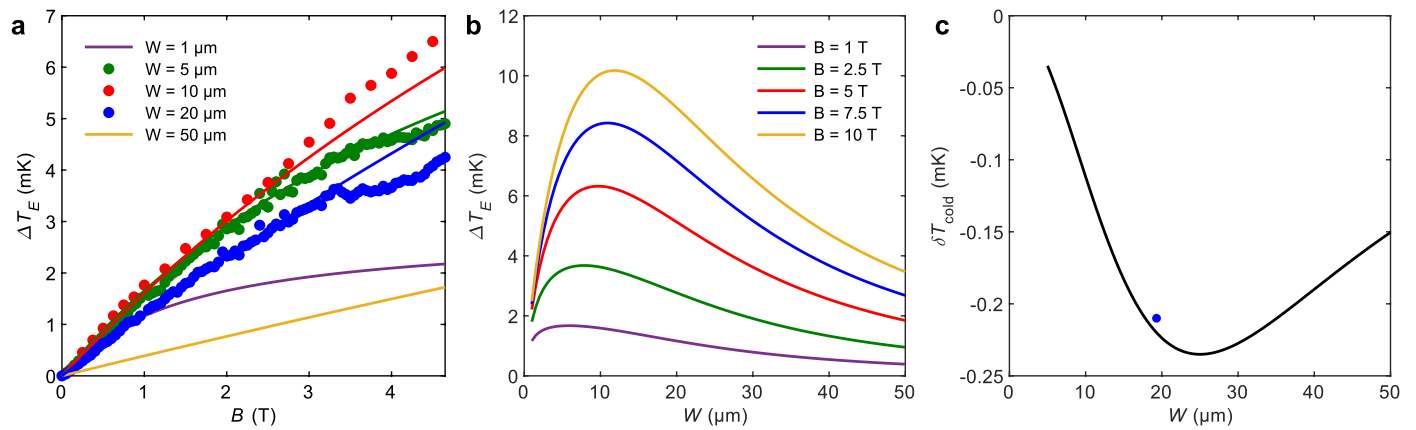
Extended Data Fig. 1 | Analytical calculations of Ettingshausen effect and absolute cooling in mesoscopic devices. (**a**) Calculated ΔT_E vs. B using Equation 11 (solid lines), fitted to the experimental data from Fig. 1l for different widths W. The calculated ΔT_E curves show the nonmonotonic dependence on W and the sublinear B dependence for small W, which becomes linear for large W. The analytical curves, based on a simplified model, are slightly different from the numerical ones presented in Fig. 1l. (**b**) Calculated ΔT_E vs. W for different magnetic field values B showing nonmonotonic W dependence. The width W for which ΔT_E is largest grows monotonically with B. (**c**) Calculated δT_{cold}^{max} (black line) showing a nonmonotonic dependence on W, peaked at W_0. The blue dot is the measured extremal δT_{cold} from Fig. 2e.
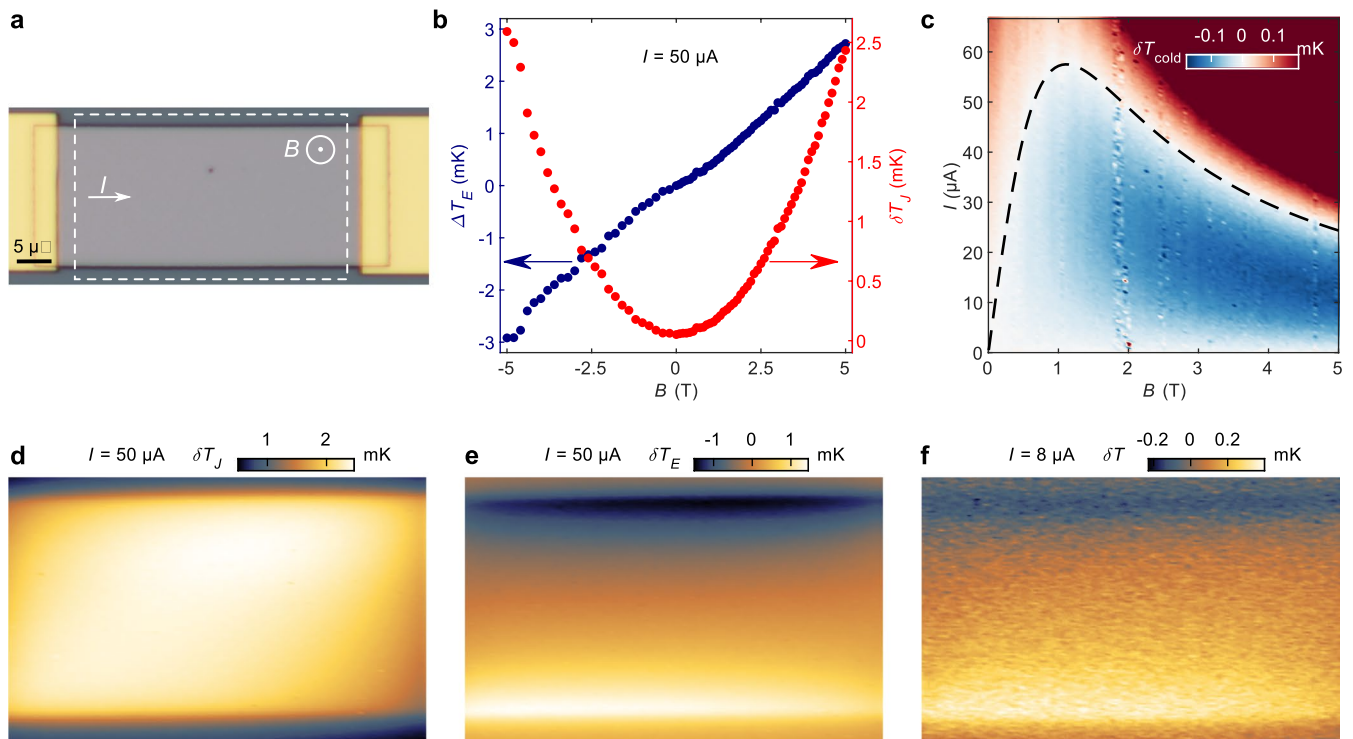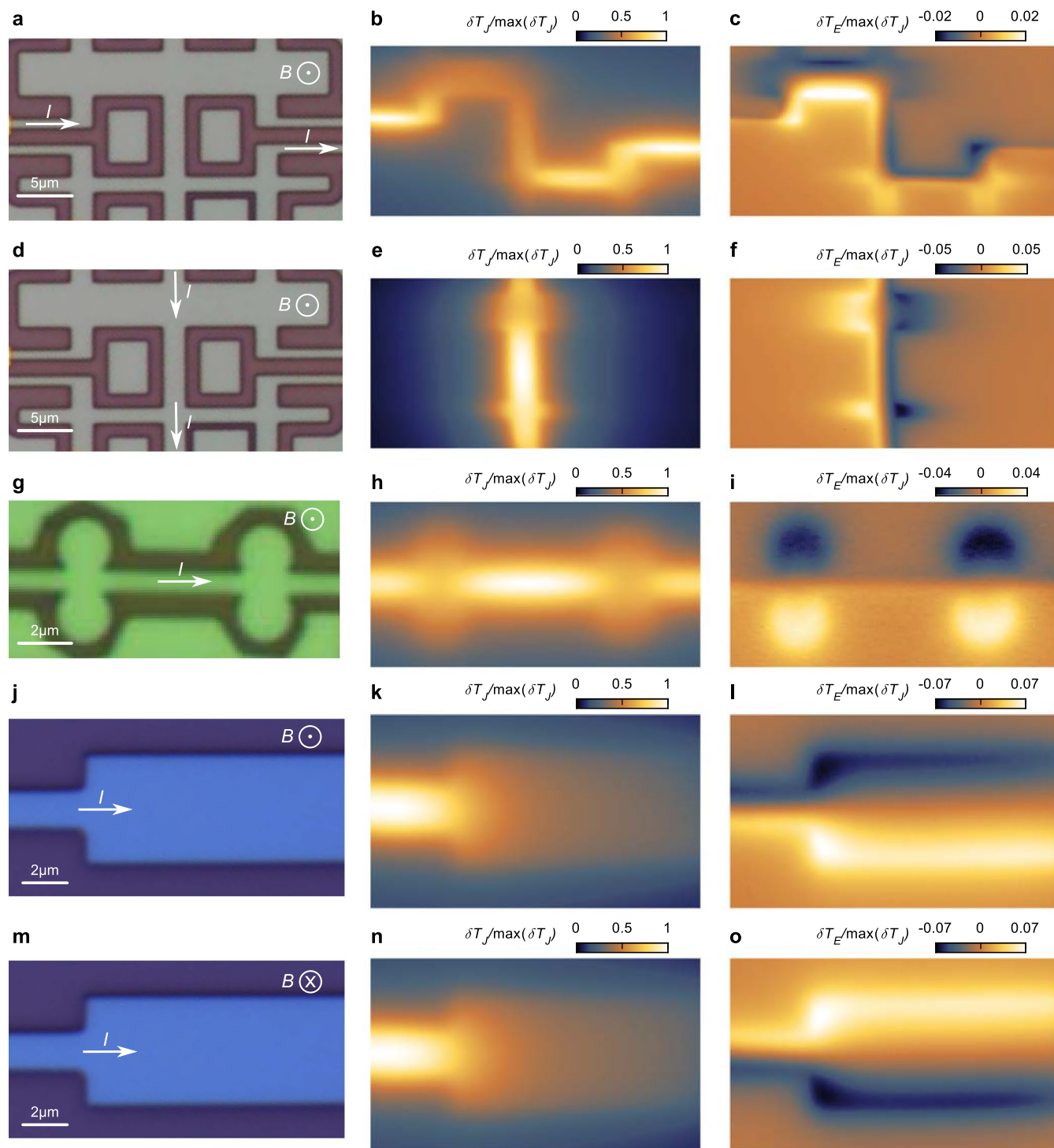
Extended Data Fig. 2 | Thermal imaging and absolute cooling in a sample with strip geometry. (**a**) Optical image of the sample with length $L = 42\,\mu m$ and width $W = 20\,\mu m$ with Au contacts on the left and right sides. (**b**) Temperature difference ΔT_E between the bottom and the top edge (blue curve) and δT_J in the center of the strip (red) vs. B at ac current of 50 µA. (**c**) The temperature of the cold edge, δT_{cold}, as a function of B and the applied unipolar current I. Dashed line shows a fit to the analytically calculated $I_0(B)$. (**d**) Thermal map of δT_J at $B = 5$T and $I = 50\,\mu A$. (**e**) Corresponding map of δT_E. (**f**) Map of the total excess temperature δT using unipolar square wave current $I = 8\,\mu A$ at $B = 5$T, revealing absolute cooling at the top edge.
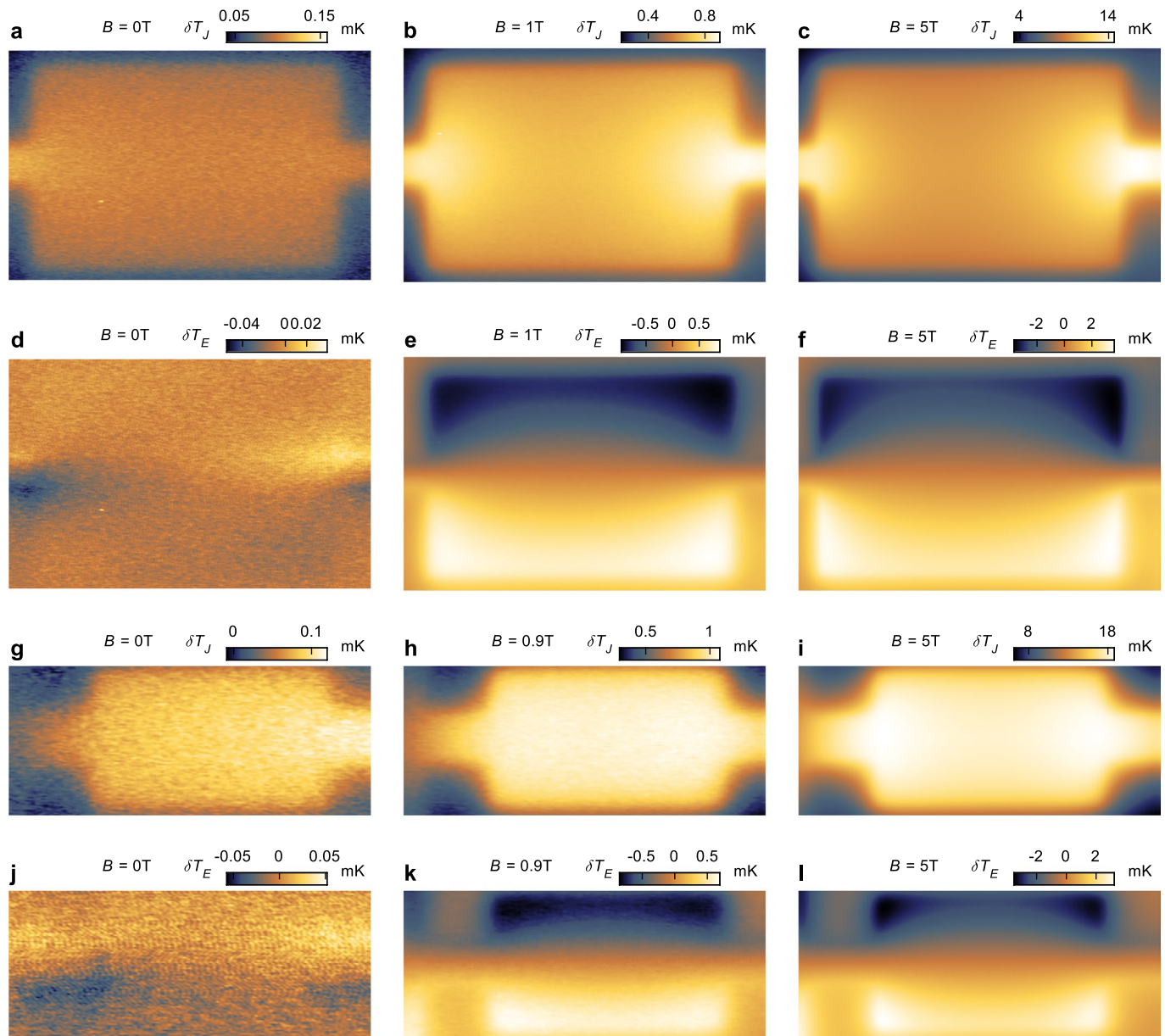
Extended Data Fig. 3 | Thermal imaging of additional chambers in rectangular geometry. (a-c) Maps of δT_J at different indicated magnetic field values for the rectangular chamber with width $W = 10\ \mu m$ at $I = 50\ \mu A$. **(d-f)** Corresponding maps of δT_E. **(g-i)** Maps of δT_J for the chamber with width $W = 5\ \mu m$. **(j-l)** Corresponding maps of δT_E.

Extended Data Fig. 4 | Thermal imaging in additional geometries. (a) Optical image of a WTe$_2$ sample with strips of different width (grey). The width of the top horizontal strip is $W = 4$ μm and of the lower strip is $W = 1$ μm. The white arrows show the current source and drain. **(b)** Thermal map of δT_J normalized by its maximal value max(δT_J) for the current flow configuration in (a). **(c)** The corresponding thermal map of δT_E normalized by the same value as in (b). **(d)** Same as a, but with a current configuration along the central vertical strip (white arrows). **(e, f)** Thermal maps of $\delta T_J/$ max(δT_J) and $\delta T_E/$ max(δT_J) respectively for the current configuration in (d). **(g)** Optical image of a WTe$_2$

sample with a narrow strip of width $W = 0.55$ μm connected to circular chambers. **(h, i)** $\delta T_J/$ max(δT_J) and $\delta T_E/$ max(δT_J) for the current configuration in (g). **(j)** Optical image of a WTe$_2$ sample with two regions of different width in series. The magnetic field $\boldsymbol{B}$ points out of the plane. **(k, l)** $\delta T_J/$ max(δT_J) and $\delta T_E/$ max(δT_J) for the configuration in (J). **(m)** Same as (j) but with $\boldsymbol{B}$ pointing in the opposite direction. **(n)** $\delta T_J/$ max(δT_J) for the configuration in (m), showing the same distribution as in (k). **(o)** $\delta T_E/$ max(δT_J) for the configuration in m, showing an opposite temperature gradient relative to (l) due to the inversion of $\boldsymbol{B}$.